

Performance Prediction Program for Wind-Assisted Cargo Ships

Martina Reche-Vilanova

DNV / DTU - Technical University of Denmark, Denmark, mrevi@dtu.dk.

Dr. Heikki Hansen

DNV, Germany.

Dr. Harry B. Bingham

DTU - Technical University of Denmark, Denmark.

Manuscript received December 21, 2021; revision received May 17, 2021; accepted May 24, 2021.

Abstract.

Wind-Assisted Propulsion Systems (WAPS) can play a key role in achieving the IMO 2050 targets on reducing the total annual GHG emissions from international shipping by at least 50%. The present project deals with the development of a six degree of freedom (DoF) Performance Prediction Program (PPP) for wind-assisted cargo ships aimed at contributing knowledge on WAPS performance. It is a fast and easy tool, able to predict the performance of any commercial ship with three possible different WAPS installed: rotor sails, rigid wing sails and DynaRigs; with only the ship main particulars and general dimensions as input data. The tool is based on semi-empirical methods and a WAPS aerodynamic database created from published data on lift and drag coefficients, which can be interpolated with the aim to scale to different sizes and configurations.

A model validation is carried out to evaluate its reliability. The results are compared with the real sailing data of a Long Range 2 (LR2) class wind-assisted tanker vessel, the Maersk Pelican. The study indicates that the PPP shows good agreement with the technology suppliers' own modelling tool and reasonable agreement with the trends of the real sailing measurements. However, for downwind sailing conditions, the predictions are more conservative than the measured values. Lastly, results showing and comparing power savings for the three different WAPS are presented. Rotor Sails are found to be the most efficient WAPS studied with a much higher potential of driving force generation per square meter of projected sail area.

Keywords: Performance Prediction Program; WAPS; Rotor sails; Rigid wing sails; DynaRig; Wind-assisted cargo ships; Sailing ships; Sail aerodynamics.

NOMENCLATURE

A	Area [m^2]
B	Beam [m]
C_L	Lift coefficient [-]
C_{L3D}	3D lift coefficient [-]
C_{L2D}	2D lift coefficient [-]
C_D	Drag coefficient [-]
C_{D2D}	2D drag coefficient [-]
C_{D3D}	3D drag coefficient [-]

C_{Di}	Induced drag coefficient [-]
C_F	Frictional coefficient [-]
C_{TF}/C_{RW}	Trailing-edge flap chord ratio [%]
D	Diameter [m]
De/D	Endplate factor [-]
d_{TF}	Trailing-edge flap deflection [deg]
e	Oswald efficiency [-]
F_D	Drag force [N]
F_L	Lift force [N]
H	Height [m]
H_S	Wave height [m]
P_S	Spinning power [W]
R	Radius [m]
R_A	Air resistance [N]
Re	Reynolds number [-]
T	Design draft [m]
T_S	Wave period [s]
U	Tangential velocity [m/s]
U/V	Velocity ratio [-]
V_s	Ship sailing speed [kn]
Γ	Circulation [m^2/s]
ρ_{air}	Air density [Kg/m^3]
ω	Angular velocity [rad/s]
AoA	Angle of Attack [deg]
AWS	Apparent Wind Speed [m/s]
AWA	Apparent Wind Angle [deg]
DM	Dyna rig mast
DoF	Degree of Freedom
DWT	Deadweight Tonnage [T]
EEDI	Energy Efficiency Design Index
GHG	Greenhouse Gases
IMO	International Maritime Organization
LOA	Length overall [m]
LPP	Length between perpendiculars [m]
LR2	Long Range 2
PPP	Performance Prediction Program
RPM	Revolutions per Minute [min^{-1}]
RS	Rotor sails
RWS	Rigid wing sails
TWA	True Wind Angle [deg]
TWS	True Wind Speed [m/s]
VPP	Velocity Prediction Program
WAPS	Wind-Assisted Propulsion Systems

1. INTRODUCTION

With the aim to respond to the current climate emergency, targets to reduce greenhouse gas (GHG) emissions are being set. The International Maritime Organization (IMO) has set its own strategy: total annual GHG emissions should be reduced by at least 50% by 2050 compared to 2008, while, at the same time, pursuing efforts towards phasing them out entirely. This has driven ship owners and operators to re-think their propulsion systems by introducing environmentally friendly fuels and

alternative propulsion technology. One green technology which is attracting a lot of attention again is wind propulsion: an old concept with a modern edge.

For centuries, wind moved cargo around the globe, until it was replaced by steam and diesel during the industrial age. Now, it is returning with a modern spin. Aeronautical technology has been implemented in wind propulsion devices to make them more efficient than traditional sails. Wind propulsion devices can be retrofitted to existent ships as a means of auxiliary propulsion power, the so-called wind-assisted propulsion system (WAPS).

After the industrial revolution and the combustion engine, research on wind propulsion gained momentum in times of high fuel prices or the prospect of a shortage of fossil fuel. During the 20th century, the most famous modern WAPS were invented. Anton Flettner, in the 1920s, invented the rotor sail (Flettner, 1926) whose performance was further studied by Thom in the 1930s (Thom, 1934). In the late 1960s, Wilhelm Prölls developed the famous DynaRig (Prölls, 1963) a modern interpretation of the square rig, which had to wait 45 years to see the light of day on the mega yacht "Maltese Falcon" (Perkins *et al.* 2004). In the 1980s, the famous French marine conservation pioneer, Jacques Cousteau, invented the Turbosail (Cousteau *et al.* 1986). Kites, on the other hand, were designed and developed for use on commercial vessels. Driven by high-performance sailing regattas such as the America's Cup, rigid wing sails have been under constant development. Most of these WAPS have been recently revived after a long "sleep" by the merchant shipping industry as a green alternative to reach environmental targets and save costs.

Velocity Prediction Programs (VPPs) to assess a sailing yacht's behaviour were initially developed during the 1970s (Kerwin, 1978). Since then, this concept has also been applied as Performance Prediction Programs (PPP) for WAPS to predict the potential fuel savings of different wind assist designs. The first examples appear in the 1980s. Schenzle (1980) and Bradbury (1981) described a PPP for a ship equipped with Dynarigs and with wing sails, respectively. Both carried out dedicated wind-tunnel tests on their corresponding ship models. The data gathered during the experiments was then used in the PPP to compute the overall performance. The results, however, were only valid for sail arrangements comparable to those tested. It is not until the commencement of the new millennium, where the interest in wind propulsion revived, that more studies on this topic were published. Smith *et al.* (2013) described an analysis process to fairly evaluate the performance of a wind-assisted ship with a set of Dynarigs using wind tunnel and CFD calculations. Burden *et al.* (2010) and Ouchi *et al.* (2013) developed PPPs for wing sails with a similar approach. Persson *et al* (2019) presented a simplified approach to model rotor and wing sails, using a limited number of 2D and 3D CFD simulations. Also, the work of Bordogna (2020) and Van der Kolk (2020), where several wind tunnel tests were carried out, was combined into a PPP capable of predicting the performance of a given wind-assisted ship with rotor sails or Dynarigs while accounting for interaction effects.

The literature shows the significant progress made on this topic. However, it also indicates that the available PPPs for wind-assisted ships are based on either expensive experimental or numerical investigations, tailored for a specific vessel or with a maximum of two different WAPS. Based on these observations, a generic performance prediction program for wind-assisted cargo ships has been developed. Its two key features, which make it different from other tools, are the small number of input data needed and its generic approach which can treat any cargo ship with three possible different WAPS installed: rotor sails, rigid wing sails and DynaRigs. It is a fast and easy tool, meant to be used at an early design stage and provide a sufficient level of accuracy, despite its generic nature, without the need to conduct project specific computational fluid dynamic simulations or experimental investigations. It is based on simple input parameters including the vessel main particulars and the dimensions of the WAPS. No specific WAPS aerodynamic data is needed - a data base is already introduced in the model. These characteristics make it the perfect tool to provide a fast answer to customers when interested in the potential of wind-assisted propulsion systems. The three included WAPS were chosen for three main reasons:

1. These devices are proven to be feasible. For instance, rotor sails are installed in presently operating commercial vessels (ENERCON, 2013; Norsepower, 2019); rigid wing sails are essentially vertical, well-established airplane wings; and DynaRigs are successfully in use on several large sailing yachts (Perkins *et al.* 2004).
2. These devices are the most likely ones to be adopted by the shipping industry due to their market availability and reference installations. Also, most of the technical papers on WAPSs in recent years have focused on the development, implementation, analysis and validation of these devices (Bordogna, 2020).
3. The limited time for this assessment. In the future, the analyses and assessment could be extended to other WAPSs, including kites and Turbosails.



Figure 1. The Maersk Pelican with rotor sails. Reprinted with permission of the copyright owner, Norsepower Oy Ltd.



Figure 2. The Oceanbird with rigid wing sails. Reprinted with permission of the copyright owner, Wallenius Marine.



Figure 3. WASP (Ecoliner) project with DynaRigs. Reprinted with permission of the copyright owner, Dykstra Naval Architects.

2. PERFORMANCE PREDICTION PROGRAM

This section introduces the Performance Prediction Program (PPP) model developed to predict the performance of wind-assisted cargo ships. A general overview of the solution algorithm and the ship model is presented.

A PPP is a mathematical model able to predict the theoretical sailing performance of a ship with specified characteristics for various wind conditions, by balancing hydrodynamic and aerodynamic forces. In other words, by balancing hull and sail forces. The method requires hull and sail characteristics as input. Results are normally presented in the form of polar diagrams. Frequently, these are, for instance, power savings or ship velocity as a function of True Wind Angle (TWA) on the radial axis and plotted for different True Wind Speeds (TWS).

For the development of this PPP for wind-assisted cargo ships, FS Equilibrium - a modular workbench from the Fluid Engineering Department of DNV; is used. All hydrodynamic and aerodynamic forces are integrated via force modules. The model has a two-part structure comprised of the solution algorithm and the ship model.

2.1 Solution Algorithm

The solution algorithm consists of an inner-loop force balance algorithm and an outer-loop trim algorithm as shown in Fig. 4. The force balance algorithm finds an equilibrium condition where the sum of the external forces, \vec{F} , and moments, \vec{M} , add up to zero in up to six degrees of freedom for the given environmental conditions. A state which fulfills these conditions is called a valid steady state and satisfies,

$$\sum \vec{F} = 0 \quad \& \quad \sum \vec{M} = 0, \quad (1)$$

The force vector $\vec{F} = (F_x, F_y, F_z)^T$ denotes the linear forces and $\vec{M} = (M_x, M_y, M_z)^T$, the angular moments. To solve Eq. 1, a balancing algorithm is used. It is a general optimization problem with constraints which can be expressed in the form,

$$\begin{aligned} \min f(x), \quad x \in \mathbb{R} \\ x_{\min} \leq x \leq x_{\max} \end{aligned} \quad (2)$$

where f is the so-called objective function and x is the vector of free variables. In a mathematical optimization, the objective function is defined as a real-valued function whose value is to be minimized. The minimization is applied to each DoF considered, using the free variable that relates to that direction. The algorithm used to perform this optimization with the equilibrium objective (minimization of force and momentum residuals) is the Newton Raphson method. In this model, these free variables are defined for each DoF as presented in Table 1.

Table 1. Free variables definition related to all six rigid-body DoF and valid range

Condition	Free Variable	Valid Range
F_x	Vs(VPP) or engine RPM(PPP)	[2-15kn] or [0-105RPM]
F_y	Leeway Angle	[-10°:10°]
F_z	Sinkage	[-0.1m:0.1m]
M_x	Heel Angle	[-10°:10°]
M_y	Pitch Angle	[-0.5°:0.5°]
M_z	Rudder Angle	[-20°:20°]

The trim algorithm in an outer-loop adjusts trim parameters to minimize an objective function such as maximizing Vs or minimizing delivered power. Trim parameters to optimize the WAPS performance are the sail Angle of Attack (AoA), flap deflection angle or the rotor sail RPM. Here, the pattern search method is employed (Hooke and Jeeves, 1961).

As shown in Table 1, the free variable utilized to minimize the residual force in the x direction is the boat speed if the velocity prediction mode (VPP) is run; or the engine RPM if it is the performance prediction mode (PPP). In VPP mode, the program finds the equilibrium condition in F_x by adjusting the free variable Vs and then maximizes Vs by optimizing the trim parameters. In PPP mode, the equilibrium in F_x is obtained with the free variable RPM and the delivered power is then minimized

by optimizing the trim parameters. Thus, VPP and PPP modes require different free variables and trim objectives. The VPP mode is normally used by yacht designers to predict maximum boat speed at various *TWS* and headings. The PPP mode is introduced to predict power savings for cargo ships with WAPS sailing at a defined speed.

Valid range limits for the free variables are set to constrain the balance algorithm to sensible values and to set limiting criteria where applicable. Table 1 shows the valid range limits used in this study. The heel angle for example is limited to +/- 10° to avoid excessive heel angles. The trim algorithm then adjusts the trim parameters so that a force balance within the heel limit is obtained.

Thanks to the open modular architecture of the FS-Equilibrium workbench, the user can set any combination of force modules, free variables, valid ranges, modes and DoF. The model enforces six DoF. For this particular application the DoF in F_z and M_y could have been omitted since the changes in sinkage and trim are very small and not all resistance effects are accounted for. The model, for example, does not account for changes in hull resistance due to trim angle. In a four DoF simulation the sinkage and trim angle would be set to fixed values while in a six DoF simulation sinkage and trim angle are adjusted to solve equilibrium in F_z and M_y . In this study the resulting sinkage and trim angle are very small and the difference in the results of a four and six DoF simulation is neglectable.

Fig. 4 shows the schematic general outline of the PPP mode.

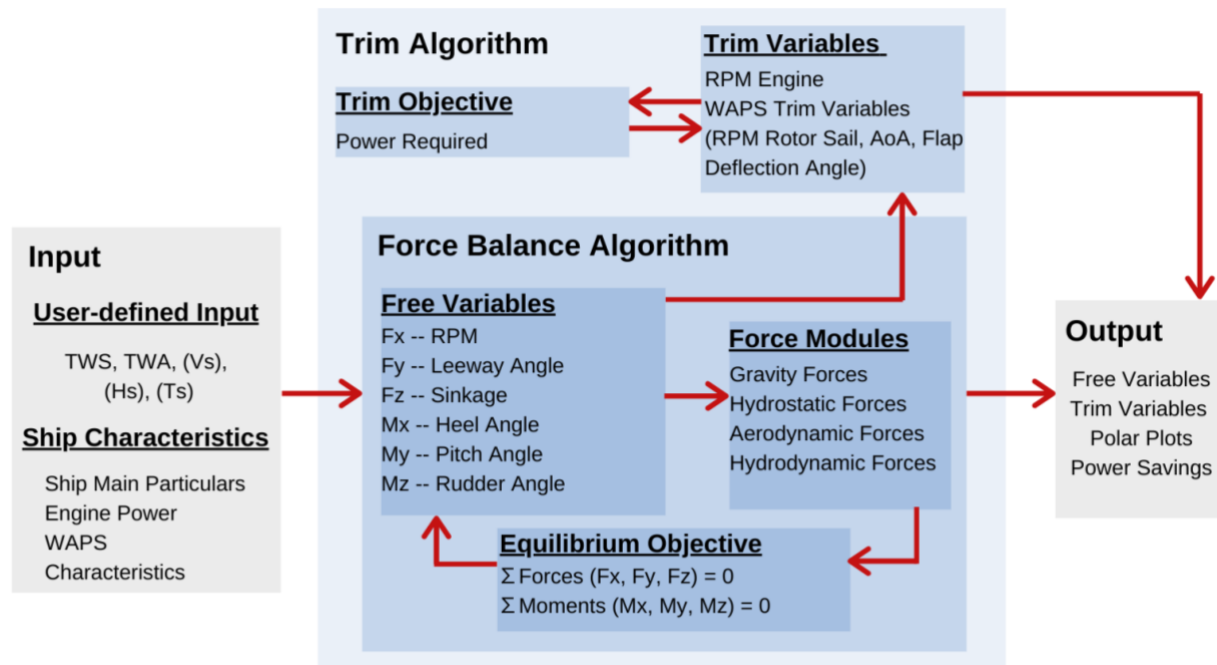


Figure 4. Schematic general outline of this Performance Prediction Program (PPP) in the FS-Equilibrium workbench.

2.2 Ship Model

The ship model comprises all hydrodynamic and aerodynamic forces and moments exerted on the wind-assisted cargo ship. These are subdivided into two: the hull model and the WAPS model. All forces and moments are described via force modules, which are computed within the force balance algorithm. The definition of each force, its respective centre of effort (CoE) and attitude effects are presented in the following sections 3 and 4.

3. HULL MODEL

This section describes the hull model, which includes all forces acting on the hull and the superstructure of the ship. The forces are described by so-called force modules, which account for the different force components.

- The mass module calculates the forces due to a non-movable mass located at a point in the body fixed coordinates, in this case, the center of gravity of the cargo ship.
- Buoyancy and hydrostatics are calculated from basic ship theory equations and approximations according to Rawson and Tupper (2001). The buoyant force is linearly dependent on sinkage, the rolling moment depends on heel and the pitching moment on pitch. The centre of buoyancy is approximated from the block coefficient and the midship coefficient, also according to basic ship theory (Rawson and Tupper, 2001). If the hull geometry is available, buoyancy and hydrostatics can be calculated from strip theory or pressure integration. To keep the required input minimal no hull geometry model was used in the examples presented in this paper.
- The hull resistance is based on the Holtrop and Mennen Method developed by a regression analysis of a collection of model experiments and full-scale data, available at the Netherlands Ship Model Basin, (Holtrop 1977 & 1984; Holtrop and Mennen 1978 & 1982). The roughness allowance is added and based on the wetted area of the hull (Holtrop and Mennen 1982; ITTC 1957). The Centre of Effort (CoE) of this force is assumed to be the centre of buoyancy. No resistance adjustment is applied for heel and pitch in this model.
- The side force, which is significant in wind-assisted ships compared to conventional ones, in response to the WAPS aerodynamic loads, and the associated drag are computed with the approach by Schenzle (1985) for sailing ships without long fin keels based on the leeway angle. The CoE of both forces is determined following the same Schenzle approach.
- The rudder hydrodynamic force module calculates the lift and drag of the rudder based on the systematic analysis of Whicker and Fehlner (1958). The x coordinate of the CoE of this force is assumed to be at 25% of the rudder chord length. The y and z coordinates are set according to its centre of area.
- The parasitic aerodynamic resistance of the superstructure is based on the drag coefficient and the frontal and lateral area of the superstructure, which is taken as the beam multiplied by the accommodation height above deck. The wind forces on the superstructure also contribute to the side force, heel and yaw moment. The CoE of this force is assumed to be the centre of area of the rectangular superstructure. The Apparent Wind Speed (AWS) and Apparent Wind Angle (AWA) are calculated at the CoE height.
- The propeller thrust, in combined and pure motor configuration, is assumed to be a Wageningen B-Screw series propeller following Kuiper (1992). Hull efficiency is approximated based on the hull type. The CoE is assumed to be the centre of area of the propeller. The propeller inflow velocity and thrust are taken along the shaft line so that the effect of leeway and pitch is considered.
- The added resistance in waves is calculated based on an in-house semi empirical method used at DNV for high-level assessment of the added resistance in a seaway. The CoE of this force is assumed to be the centre of buoyancy.

4. WAPS MODEL

In this section three different WAPS models are presented: Rotor sails, rigid wing sails and DynaRigs. The configuration, the aerodynamic loads prediction and the corresponding data sources for each device are detailed. At the end of the section, interaction assumptions for multiple operating WAPS are mentioned.

The WAPS models are based on an aerodynamic database created from published data on lift and drag coefficients, which can be interpolated with the aim to scale to different sizes and configurations. The reference height for *TWS* and *TWA* are at 10 m above the still water level. *AWS* and *AWA* are calculated at the CoE of each WAPS considering heel and pitch. *AWS* and *AWA* are calculated from the flow components in the heeled and pitched plane perpendicular to the span direction of the device following the effective angle theory for sail aerodynamics as described for example by Hansen (2008). For small heel and pitch angles this effect is however neglectable. The true wind velocity profile as a function of height is assumed to be an exponential gradient with exponent 0.11. Note that the valid range of each WAPS model is determined by the data source valid range used, which could conceivably expand in the future if additional data sets are included.

4.1. Rotor Sails Model

The model can predict any rotor sail configuration within the valid range shown in Table 1. Note that the aspect ratio of a rotor sail is defined as the ratio of its height to its diameter. The maximum spinning RPM limit is set depending on the rotor size and implementation for each vessel.

Table 1. Rotor sails configurations and their respective valid ranges.

Symbol	Configuration Parameter	Valid Range
<i>AR</i>	Aspect ratio (Height/Diameter)	[1.68:12]
<i>De/D</i>	Endplate size factor	[1:3]

The CoE of the forces presented in this section is assumed to be at the centre of area of each rotor. The x and y coordinates are the position of the rotation axis and the z coordinate is taken at half way up the rotor.

4.1.1 Aerodynamic Loads

The Magnus effect, named after Gustav Magnus, Professor of Physics at the University of Berlin from 1834 to 1869, is the phenomenon responsible for the lifting force generated by rotor sails. On a rotating cylinder, it can be described by the superposition of two simple flows: the free-stream parallel flow and the circulatory flow. On one side of the cylinder, where the streamlines move in the same direction as the flow created by the rotor, the resultant flow is the sum of a parallel and a circulatory flow; whereas on the other side, the resultant flow is the difference between them. Due to this velocity difference between the rotating cylinder sides, a pressure distribution over the device appears, manifesting a lifting force which tends to push the cylinder in the direction of lower pressure. See Fig. 5 for reference.

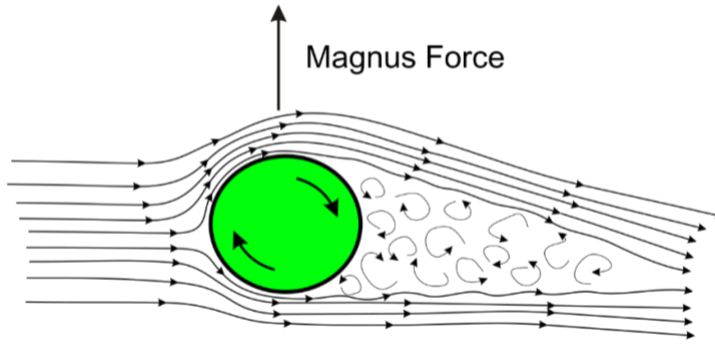


Figure 5. Magnus effect seen in a rotating cylinder. The vertical arrow represents the resulting lift force. Reprinted from Rdurkacz (2013). Reprinted with permission.

The total aerodynamic force acting on the rotor sail due to the Magnus effect can be calculated from the lift and the drag. The lift is the force perpendicular to the incoming flow, defined as,

$$F_L = \frac{1}{2} \rho_A AWS^2 A C_L, \quad (3)$$

where ρ_A is the air density, AWS is the apparent wind speed, $A = H D$ is the planform area of the cylinder, and C_L is the lift coefficient. The drag is the force parallel to the incoming flow, defined as,

$$F_D = \frac{1}{2} \rho_A AWS^2 A C_D, \quad (4)$$

with C_D as the drag coefficient. Neglecting energy dissipation, a theoretical lift coefficient value can be derived by substituting the expression of lift for the dimensionless lift coefficient into the Kutta-Joukowski theorem of lift equation defined as (Newman, 2017),

$$F_L = \rho_A \Gamma AWS H \quad (5)$$

where Γ is the circulation induced by the spinning cylinder and H is the cylinder height. Assuming that $\Gamma = 2\pi R U$ where $U = \omega R$ is the velocity of the cylinder surface and ω the rotation rate gives a theoretical ideal fluid lift coefficient of,

$$C_L = 2\pi U/V, \quad \text{where } U/V = \frac{\omega R}{AWS} \quad (6)$$

is the velocity ratio. This theoretical value does not consider viscosity. Empirical coefficients in real fluids are much lower. The drag coefficient cannot be derived from ideal fluid theory. It can only be established empirically. However, what is clear is the dependency of the lift coefficient on the rotor sail velocity ratio. This correlation is responsible for its inherent reefing capability. According to Eq. 6, if we hold the spin velocity fixed due to a realistic maximum operating RPM, any increase in AWS results in a decrease of C_L . Since the lift force is a function of both AWS and C_L , the two changes reduce the quadratic growth rate of this force with AWS to a linear growth.

4.1.2 Data Source and Data Fitting

In the history of the study and development of rotor sails and Magnus effect applications, several engineers and physicists carried out experiments with the aim to determine lift and drag coefficients. All these studies obtained different results because of their different rotor configurations. However, most of them were inside an envelope between 25% and 50% of the theoretical lift coefficient. In this project, no wind tunnel tests were carried out because of its aim to develop a general model which

can work for all rotor sail configurations within the valid range. Thus, public sources are used. It was decided to use the Jakob Ackeret results from Prandtl and Betz (1932) for two main reasons: its wide acceptance as high-quality data inside the scientific community and its high velocity ratio range (up to 8 when most of the sources are up to 4). The Ackeret results are based on the measurement of lift and drag coefficients as a function of velocity ratio for two cylinders, one with aspect ratio of 1.68 and the other with aspect ratio 12. Also, endplate size was varied. Normally, endplates are defined as a function of their diameter factor De/D (end plate diameter/ rotor diameter). Ackeret carried out wind tunnel tests for De/D of 1, 1.5, 2 and 3 for each aspect ratio. His findings are summarized in Fig. 6.

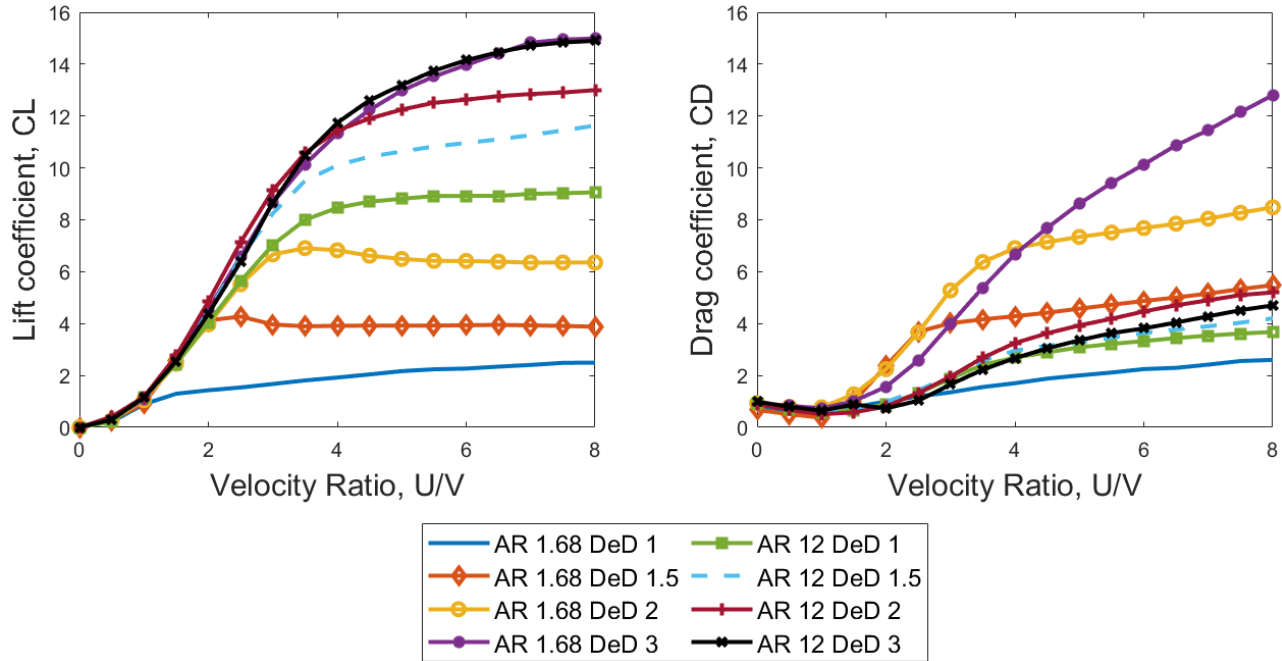


Figure 6. Ackeret lift and drag coefficients according to Prandtl and Betz (1932).

With the aim to improve the interpolation accuracy and, therefore, the model predictions, wind tunnel test results from the retrofitted cargo ship Fehn Pollux (Vahs, 2019) are also included in this rotor sail model data set. To predict the aerodynamic loads of any rotor sail within the valid configuration range, the discrete data is fitted with a multi-dimensional spline interpolation, integrated into the FS-Equilibrium software. No extrapolation is considered. See Fig. 7 for an example.

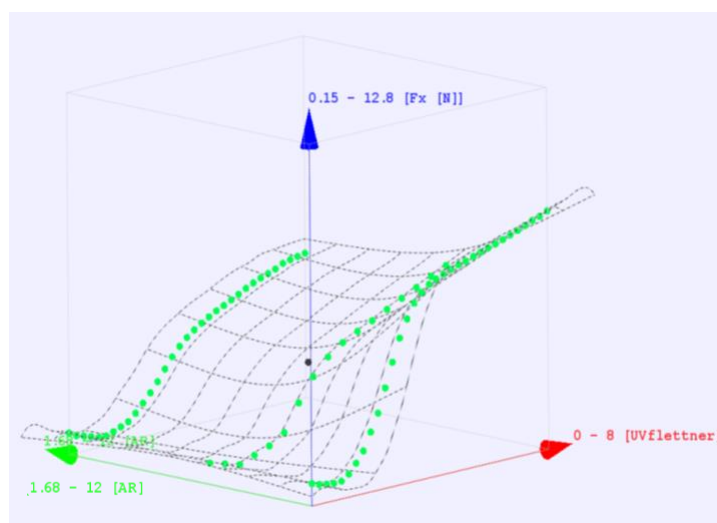


Figure 7. Rotor sails drag coefficient data fitted with multi-dimensional spline interpolation.

The three data variables of this model are:

- The aspect ratio, AR . With a valid range from 1.68 to 12.
- The endplate size factor, De/D . With a valid range from 1 to 3.
- The velocity ratio, U/V . With a valid range from 0 to 8.

These variables are based on the effects on the aerodynamic coefficients considered in this model: the aspect ratio, the endplate size and the velocity ratio. Others such as span wise disks, surface roughness and Reynolds number; are neglected. Span wise disks and surface roughness lead to higher maximum lift coefficients compared to smooth plain rotor sails. The trade off, however, is the additional spinning power required due to higher friction. The sum of these effects does not significantly affect the overall performance of the considered rotor sail configuration (Seifert, 2012). Due to this and other practical considerations, commercially available rotor systems use a smooth surface finish without increased surface roughness. The Reynolds number has a considerable impact on the lift coefficient in the critical flow region and below velocity ratios of 2.5. Conversely, the drag coefficient is markedly influenced by the Reynolds number in the velocity ratio range $1 < U/V < 2.5$ (Bordogna *et al.* 2019). The Reynolds number effect on lift and drag at higher U/V ratios, which are typically used during operation to achieve optimal aerodynamic performance, is not significant and is therefore not considered. The Reynolds number at these higher U/V ratios is at least 10^6 . Nonetheless, note that Reynolds effects could have a considerable impact on the results for lower U/V ratios.

4.1.3 Spinning Power

Unlike the other two WAPS presented in this paper, rotor sails are active-rotating devices. Thus, the required spinning power due to frictional drag must be accounted for in order to have an accurate and fair model. Here we assume that mechanical losses in the drive and bearings are negligible compared to those due to aerodynamic skin-friction. The tangential viscous force on the spinning cylinder can be estimated from flat plate boundary layer theory (Schlichting 1979; Newman, 2017; Bordogna, 2020). The required power then equals the tangential frictional force times the tangential velocity U , and it can be written

$$P_S = \frac{1}{2} \rho_A U^3 \pi H_{RS} D_{RS} C_F, \quad (7)$$

where $(\pi H_{RS} D_{RS})$ is the surface area of the cylinder with H_{RS} and D_{RS} the cylinder height and diameter, respectively. The skin-friction drag coefficient, C_F , is approximated from the experiments of Schlichting (1979), which are parametrized by,

$$C_F = (2 \log_{10}(Re) - 0.65)^{-2.3} \quad \text{for } Re < 10^9, \quad (8)$$

where the Reynolds number is computed from D_{RS} and U . The power consumption thus scales with the cube of the tangential velocity and is independent of the wind speed. As an indication that this is a reasonably accurate approach, we note that Bordogna *et al.* (2019) measured an average value of $C_F = 0.007$ for their experiments over the range $10^5 < Re < 10^6$ where Eq. (8) gives a value of approximately 0.0055. Since their measurements included mechanical friction, and were done at relatively small scale, it seems likely that the difference represents the mechanical losses. They also concluded that C_F is independent of wind speed. End plates can also be included in the total spinning power required by adding their corresponding surface area into Eq. 7.

4.1.4 Air Resistance

When the rotor sail is not rotating, in pure motor configuration where the engine is the only source of propulsion; and assuming non-retractable devices, its structure creates air resistance but no lift. This resistance is modelled here by,

$$R_A = \frac{1}{2} \rho_A A W S^2 H_{RS} D_{RS} C_D. \quad (9)$$

This force is only considered in the x and y directions - z is neglected. The drag coefficient, C_D , is assumed to be 0.5 (2D circular shape value for Re of 10^6 according to NASA (2015)).

4.2. Rigid Wing Sail Model

The rigid wing sail model can predict the performance of three different configurations: a plain symmetric profile and a symmetric profile with a trailing edge plain flap or a slotted flap; as seen in Fig. 8. The size of the flap (expressed relative to the chord length of the symmetric profile) and the maximum flap angle are defined by the user.

As in the rotor sails model, the rigid wing sail model has some bounds on the configuration of these three possible devices, which are shown in Table 2. There is no limitation for AR which is defined as the ratio of its height to its chord length.

Table 2. Rigid wing sail configurations and their respective valid ranges.

Symbol	Configuration Parameter	Valid Range
d_{TF}	Flap deflection	[0° : 45°]
C_{TF}/C_{RW}	Flap chord ratio	[0% : 30%]

The x and y coordinates of the CoE of the forces presented in this section is set at the 25% chord length of the rigid wing sail when aligned with the centreline. The z coordinate is assumed to be at half of the total sail height. The variation of the longitudinal and lateral position of the CoE due to rotation of the wing sail and camber from the flaps is assumed negligible – the variance with respect to the *LOA* of the ship is minimal.

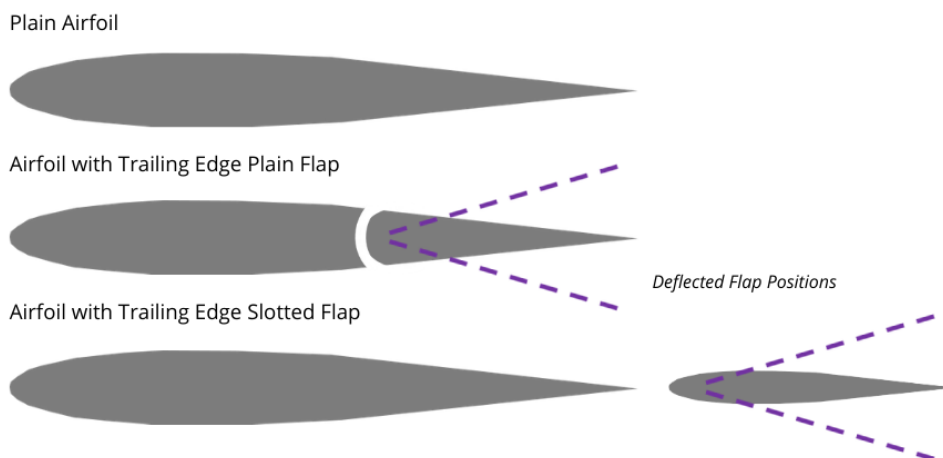


Figure 8. Rigid wing sail model configurations.

4.2.1 Aerodynamic Loads

Rigid wing sails can deliver a thrust force by means of a lift force generated by the motion through the air. In addition, a force along the flow direction of the sail, drag, is always present. From the linearized 2D form of Bernoulli's equation and the Kutta-Joukowski theorem (Newman, 2017; Abbott and Von Doenhoff, 1959), both aerodynamic forces can be expressed in non-dimensional form as,

$$\frac{F_L}{0.5 \rho_A AWS^2 A} = C_{L2D} (Re, AoA), \quad (10)$$

$$\frac{F_D}{0.5 \rho_A AWS^2 A} = C_{D2D} (Re, AoA). \quad (11)$$

Aerodynamic forces vary directly with air density, the square of the apparent wind speed and the total airfoil area. Both aerodynamic coefficients depend on the Reynolds number, Re , and the angle of attack, AoA . For the simplest airfoil case, a flat plate, with an AoA , the lift coefficient is defined as,

$$C_{L2D} = 2\pi AoA. \quad (12)$$

Thus, the lift coefficient of a flat plate is 2π times the AoA in radians. Plotting the coefficient against the angle of attack is a convenient way of describing the aerodynamic characteristics of a rigid wing sail. The lift increases almost linearly with angle of attack until a maximum value is reached, whereupon the wing is said to "stall". The drag coefficients have a minimum value at a low lift coefficient, and the shape of the curve is approximately parabolic at angles of attack below stall. See Fig. 9 for an example.

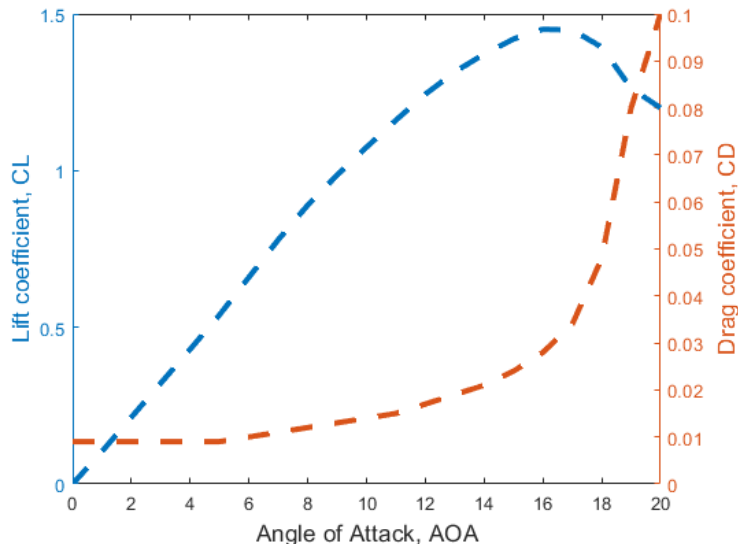


Figure 9. NACA 0012 simple airfoil 2D lift and drag coefficients.

The ideal wing gives high lift for minimum drag. A rigid wing sail configuration can be improved by use of some high-lifting devices such as trailing-edge flaps. When deflected, these systems are responsible for an effective camber generation in the airfoil. Unlike thickness, camber plays a role in the magnitude of the lift coefficient. The cambered parabolic arc represents a substantial improvement over a flat plate from the standpoint of uniform loading and pressure distribution. This effect on the total lift coefficient is expressed in the form,

$$C_{L2D}(AoA) = C_{L2D}(0) + 2\pi AoA, \quad (13)$$

where the term $C_{L2D}(0)$ represents the effects of camber at 0 AoA , and $2\pi AoA$ represents the effect of the angle of attack.

Generally, the center of pressure of a symmetric airfoil is assumed to be at 25% of the chord length (Newman, 2017; Abbott and Von Doenhoff, 1959). In 3D, the flow at each section along the span of the rigid wing sail can be approximated as 2D. However, at the tips, due to pressure leakage, vortices appear. The effects are twofold: the lift is reduced, and the drag increased. The AR of the airfoil plays a significant role on the total aerodynamic load. A large AR wing means that the flow is nearly independent of the transverse coordinate z and a 2D approximation is valid. On the other hand, for lower AR , 3D flow effects are important and must be included.

4.2.2 Data Source and Data Fitting

The lift and drag prediction model for rigid wing sails is divided into two main parts: 2D and 3D prediction. The 2D approximation accounts for the profile shape and the camber effect while the 3D one modifies the 2D result to account for the effects of aspect ratio and tip vortices. Wing-ship interference and profile thickness effects are not considered in this model due to their negligible effects on the lift coefficient.

The 2D profile data (lift and drag coefficients as function of AoA) is obtained from the NACA 0012 symmetric profile. NACA symmetric profiles are widely used in rigid wing sail applications as they can generate lift on either side. Typical commercial wing sails tend to be in the range of 12% to 18%, and since the maximum lift to drag ratios do not change much over this range, a 12% thickness is selected as representative. The effect of camber, due to trailing-edge plain or slotted flap implementation; on lift and drag coefficients for profiles with flaps is determined using the DATCOM 1978 method (Finck, 1977) and the approximation of Young (1953). These sorts of high-lift devices, for instance, increase lift for 0° AoA while reaching a higher maximum lift coefficient but a lower stalling angle. See Fig. 10 for reference. Note that the model is designed to only predict the pre-stalled performance of flapped sails.

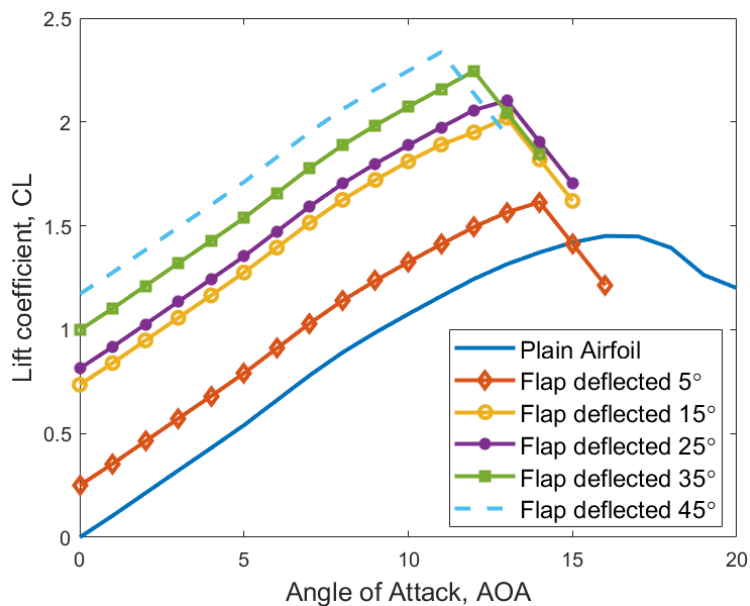


Figure 10. 2D lift coefficients of a NACA 0012 with 30% chord length trailing edge plain flap with variable flap deflection. Note that post-stalling performance is not accurate.

The 3D model accounts for downwash reducing lift and induced drag due to spillage around the wing tips. It also accounts for different aspect ratios. These effects are modelled according to Prandtl's lifting line theory (Newman, 2017; Abbott and Von Doenhoff, 1959). 3D lift and drag coefficients are derived as,

$$C_{L3D} = \frac{C_{L2D}}{1 + \frac{C_{L2D}}{AR\pi}}, \quad (14)$$

$$C_{D3D} = C_{D2D} + C_{Di} = C_{D2D} + \frac{C_{L3D}^2}{AR\pi e}. \quad (15)$$

The 2D drag coefficient accounts for skin friction and wing section shape at zero lift whereas the 3D one also considers the induced drag produced at the wing tips due to lift generation. For high aspect ratio rigid wing sails, both 3D aerodynamic coefficients tend to their respective 2D values. The Oswald efficiency, e , depends on the lift distribution. For an elliptic lift distribution, it gets its maximum value of 1.

All data is loaded into the developed model in the PPP. It is fitted to find the right values for each given input condition, such as flap dimensions, utilizing a multi-dimensional spline of the discrete input data. No extrapolation is considered. The three data variables of this model are:

- Angle of attack, AoA . With a valid range from 0° to 90° .
- Flap deflection, d_{TF} . With a valid range from 0° to 45° .
- Flap chord ratio, C_{TF}/C_{RW} . With a valid range from 0% to 30%.

The AoA valid range is up to 90° , where the downwind condition large $AoAs$ is modelled according to plain airfoil wind tunnel test data in Schenzle (1980).

4.2.3 Air Resistance

Rigid wing sails are assumed retractable since most of the commercial options available in the market are foldable when not in use. The PPP determines when it is beneficial to retract the rigid wing sails. Thus, no separate air resistance for the wing in the feathered condition is modelled for these devices. For partially retractable wings, it can be modelled following Eq. 9.

4.3. DynaRig Model

The DynaRig model can predict any sail configuration with an approximate aspect ratio of 2, which is defined as the ratio of its height to its chord length. This valid range is in line with the generic aspect ratio, between 1.5 and 2, of most DynaRigs.

The CoE of these sails sits just forward of the mast and near the centerline of the vessel for an optimum performance in trimming (Perkins *et al.* 2004). The z coordinate is assumed to be at half of the total sail height.

4.3.1 Aerodynamic Loads

The DynaRig is a soft cambered sail which generates aerodynamic loads following the lift and drag generation principle described as,

$$F_L = \frac{1}{2} \rho_A AWS^2 A C_L, \quad (16)$$

where ρ_A is the air density, AWS is the apparent wind speed, A is the planform area of the DynaRig, and C_L is the lift coefficient. The drag is the force parallel to the incoming flow, defined as,

$$F_D = \frac{1}{2} \rho_A AWS^2 A C_D, \quad (17)$$

with C_D as the drag coefficient. C_L and C_D are for the 3-dimensional flow and are determined for the relevant aspect ratios.

4.3.2 Data Source and Data Fitting

Since Prölss invented the DynaRig back in the sixties, a number of wind tunnel tests have been carried out in order to evaluate the performance of these sails such as Perkins *et al.* (2004), Smith *et al.* (2013) and Bordogna (2020). The Perkins *et al.* (2004) results presented aerodynamic coefficients for the high tech DynaRigs of the "Maltese Falcon" mega yacht with a higher aspect ratio, which are unrealistic values for WAPS applications in cargo ships. The Smith *et al.* (2013) results, which include interaction effects, are only valid for sail arrangements comparable to those tested. For these reasons, the data source used in the model is from Bordogna (2020). The Bordogna wind tunnel tests used a DynaRig with an *AR* of 1.85 and a camber of 10%. The rig was virtually trimmed via a computer program which optimized the maximum thrust for each *AWA*. Bordogna studied the aerodynamic performance of a single DynaRig and two DynaRigs with a horizontal distance between the two masts relative to sail chord of 2.5 and 4.

The Reynolds number effect is assumed negligible in this model. The data is fitted following a spline interpolation in this model. The *AoA* valid range is from 0° up to 90°.

4.3.3 Air Resistance

When the DynaRig does not produce forward thrust, the sails can be completely reefed. In this sailing configuration, where the engine is the only source of propulsion; and assuming non-retractable masts, the air resistance of the DynaRig structure is modelled here following:

$$R_A = \frac{1}{2} \rho_A AWS^2 H_{DM} D_{DM} C_{DM}. \quad (18)$$

C_{DM} is assumed to be 0.5. Generic circular shapes have C_D 0.5-0.7 according to NASA (2015). This force is only considered in the x and y directions - z is neglected. The yards, assumed to be trimmed while sailing in pure motor configuration to produce minimum resistance, are defined as negligible here with the aim to simplify the model. Thus, the mast is responsible of most of the total real air resistance of the non-retractable DynaRig structure.

4.4 Interaction Effects

Assuming that in wind-assisted cargo ships the devices will be installed far enough apart to be able to operate independently, no interaction effects are considered in this model. According to Bordogna *et al.* (2019), when rotor sails are spaced 15 diameters apart, the interaction effects are very small. However, when they are spaced 3 diameters apart, interaction effects include changes in the aerodynamic coefficients of up to 20% with respect to the single rotor sail values. Generally, the aerodynamic coefficients of several rotor sails operating together are considerably influenced by their relative position, spacing and velocity ratio (Bordogna *et al.* 2019). For multiple rigid wing sails

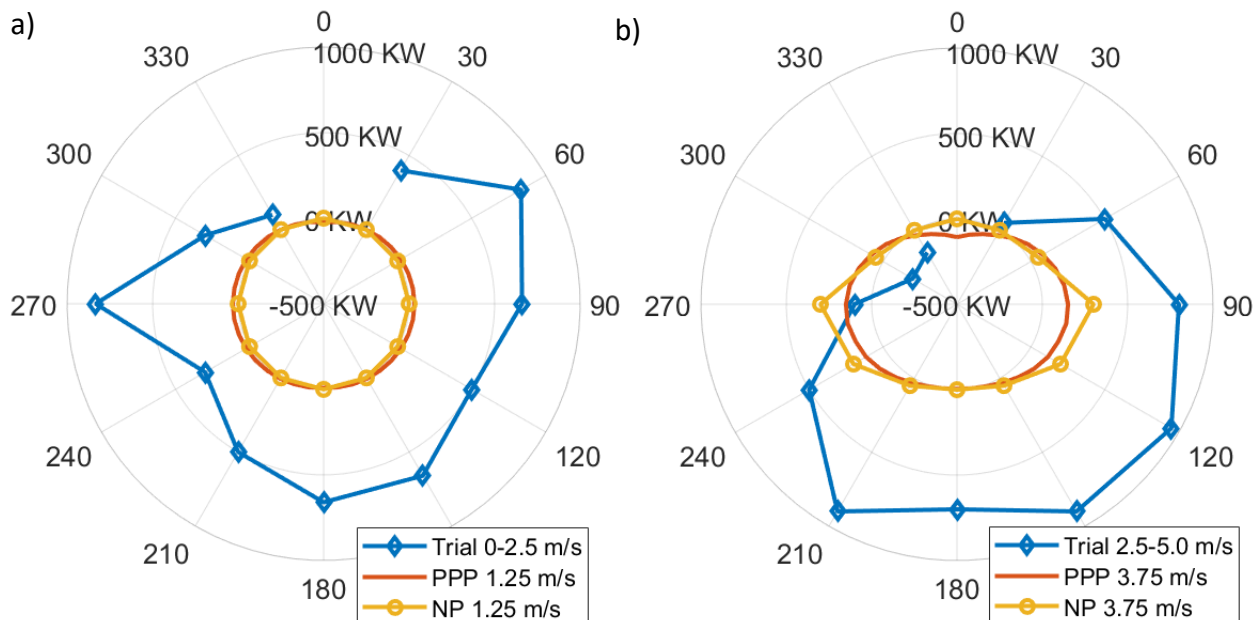
and DynaRigs the main influencing factors are their relative position, spacing, the angle of attack (trim) and camber (Perkins *et al.* 2004; Chapin 2015; Bordogna 2020).

5. VALIDATION – MAERSK PELICAN

This section presents and discusses the validation of this PPP. The Long Range 2 (LR2) class tanker vessel “Maersk Pelican”, fitted with two 30 meter high rotor sails in 2018, is used as the validation ship. Maersk Pelican is the world’s largest cargo vessel using wind-assisted technology. The vessel is 244.6-m *LOA*, 233-m *LPP*, 42.03-m *B*, 15.45-m *T* and 109,647-t *DWT*. Its engine power is 15,260 kW with a design speed of 15.3 kn.

The real sailing performance data, provided by the sail technology provider of “Maersk Pelican”, Norsepower, was continuously acquired for one year by independent ship performance specialists from Lloyd’s Register (Paakkari *et al.* 2020). Most of the trial data set was collected between 11.5–13.5 kn ship speeds. Polar diagrams of the net propulsion power saved as a function of True Wind Speed, *TWS*, over the ranges: 0-2.5 m/s, 2.5-5 m/s, 5-7.5 m/s, 7.5-10 m/s and 10-12.5 m/s; along with True Wind Angle, *TWA*, relative to the bow were built. No valid data was found in *TWAs* between 330° to 30° partly because the rotor velocity ratio, *U/V*, was reduced below 50 RPM and therefore excluded from the plots. The real sailing diagrams are representative of average corrected trial data points for a ship speed through water of 12.5 kn and all load conditions (Paakkari *et al.* 2020). Together with the Norsepower performance predictions, power savings results are compared with those obtained from the program developed here. The *TWS* of each simulation is set as the mid value of each trial *TWS* range in both the Norsepower and our own performance predictions.

To achieve comparable results, the same main particulars and rotor dimensions are loaded into the model for the same loading and speed conditions. Power savings are computed in the PPP by subtracting the required delivered power of the wind-assisted ship (two 30x5-m rotor sails) from the conventional motor ship (without rotor sails onboard). The power required to spin the rotors and their air resistance (if not rotating) are accounted for. The model checks the optimal rotating condition of the rotor sails to maximize savings by trimming rotor RPM constantly. Both rotors are assumed to spin at the same RPM. Interaction between them is not accounted for. The results are plotted against Norsepower (NP) predictions and the real trial data in Fig. 11 as a function of *TWS* and *TWA* relative to the bow.



See the next page for figure cation

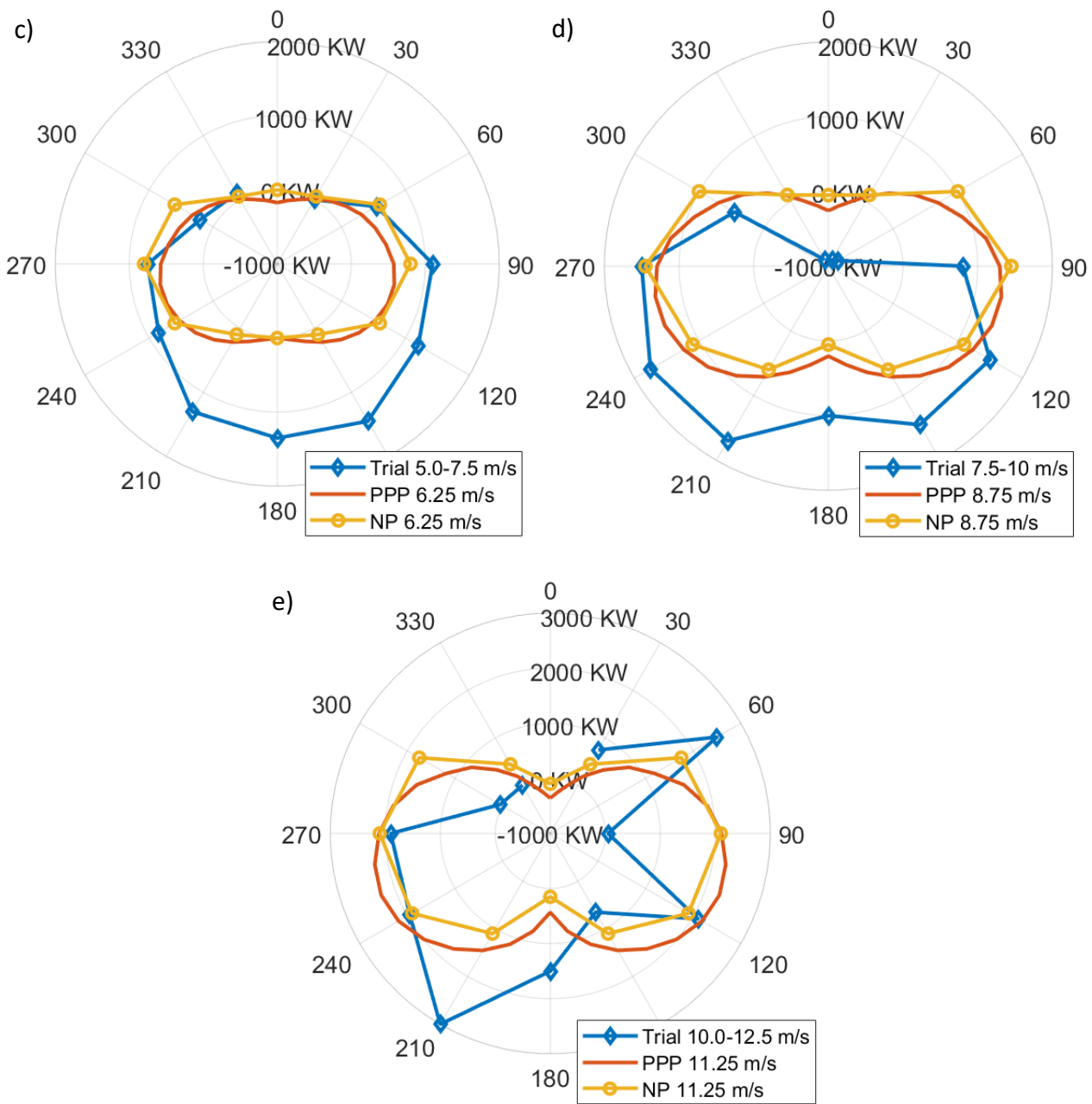


Figure 11. Trial data vs our PPP vs Norsepower (NP) estimated total propulsion saving polar diagrams as a function of TWS and TWA relative to the bow of Maersk Pelican rotor sail vessel. NP and Trial results reproduced with permission of the copyright owner, Norsepower Oy Ltd.

The PPP developed here shows similar results to the Norsepower (NP) predictions for all TWS tested. Generally, the predicted performance seems to be higher upwind for NP and higher downwind for the PPP. Another noticeable difference is that the NP results for 0° TWA do not show negative savings, which indicates that windage is not accounted for when the rotor does not produce forward thrust. The PPP is also seen to match the trial data for some ranges. The air resistance in the upwind condition ($TWA = 0^\circ$) is clearly seen from the obtained PPP negative power savings - higher delivered power is required than without rotor sails installed. Despite the lack of data for the upwind condition in the trial data, the same trend is seen for $TWS 7.5-10 \text{ m/s}$. On the other hand, the model does not show the large forces coming from the trial data in the downwind condition ($TWA = 180^\circ$). Considering, for example, a downwind condition ($TWA = 180^\circ$) at a TWS of 6.25 m/s (12.15 kn) with the ship sailing at 12.5 kn (See Fig. 11c for reference), where, the resultant AWS half

way up the rotor sail is only 1.5 kn (2.1kn at the top of the rotor sail) when assuming an exponential true wind velocity gradient with exponent 0.11. In this case, no significant power savings due to the rotors would be expected.

Given the limited data in some sailing conditions, there is some uncertainty in the trial results. Some of the points may therefore be seen as observed values rather than the long-term expectation. Also, both NP and PPP results represent the predicted power savings for the mid value of each trial TWS range, while the trial data represent the average of all data within the range.

All in all, the results, show a fair agreement despite all the measurement uncertainties and given the generic approach and purpose of the PPP developed here. For future development, more data could be studied and compared and also for other WAPS.

6. EXAMPLE APPLICATION

This section presents a case study aiming at showing the energy savings potential and the main differences in performance between the three WAPS available in the model: rotor sails, rigid wing sails and DynaRigs. The cargo ship used to perform these calculations is the ‘Maersk Pelican’. Thanks to their available deck space, tankers and bulk-carriers are especially suitable for wind propulsion. Also, due to their low design speed, it is more challenging for these ships to fulfill the requirements of the Energy Efficiency Design Index (EEDI).

The first challenge when comparing the performance of each WAPS is selecting their total sail areas which are key to generating a similar forward thrust for a given wind and sailing conditions. Otherwise, the results are difficult to interpret. The required difference in size will also provide the efficiency of each WAPS in terms of forward thrust per square meter of projected sail area. To do so, a PPP calculation is conducted for one of the two 30x5m rotor sails with $De/D = 2$ installed midship for the reference sailing condition. The TWS is defined as 10m/s, the annual average value in the North Atlantic (Schenzle, 1983). The ship speed is taken as 12.5kn, the mean real service speed of the ‘Maersk Pelican’ (Paakkari *et al.* 2020).

Comparing lift coefficients and assuming the same aspect ratio of 2 for both rigid wing sails and DynaRig, the area needed for each WAPS to match the rotor sail lift generation at maximum forward thrust is computed. The performance efficiency of each device is given as a factor of lift force generated per projected sail area. The results, normalized to the least efficient device, are shown in Table 5. Note that the maximum forward thrust occurs at a different TWA for each WAPS. C_{L3D} in Table 5 is the maximum value for the given WAPS configuration.

Table 5. WAPS efficiency comparison.

WAPS	C_{L3D}	Area [m²]	Efficiency [N / m²]	Normalized Efficiency
Rotor sail (AR=6 De/D=2)	9.15	150	650.37	7.76
Rigid wing sail no flap (AR=2)	1.18	1163.47	83.45	1
Rigid wing sail 30% plain flap (AR=2)	1.70	807.59	120.80	1.44
Rigid wing sail 30% slotted flap (AR=2)	1.73	793.58	122.93	1.47
DynaRig (AR=2)	1.48	927.63	105.17	1.25

Table 5 shows the considered WAPS parameters and their efficiency in generating a lift force per square meter of projected sail area. This illustrates how rotor sails generate the most lift force per projected sail area, ~8 times higher C_L than a rigid wing sail without flaps. However, the rotor sail’s

tradeoff is the required spinning power. Also, the flap's potential of achieving much higher lift generation is clear. Fig. 12 visualizes this lift generation comparison by showing the different resulting areas.

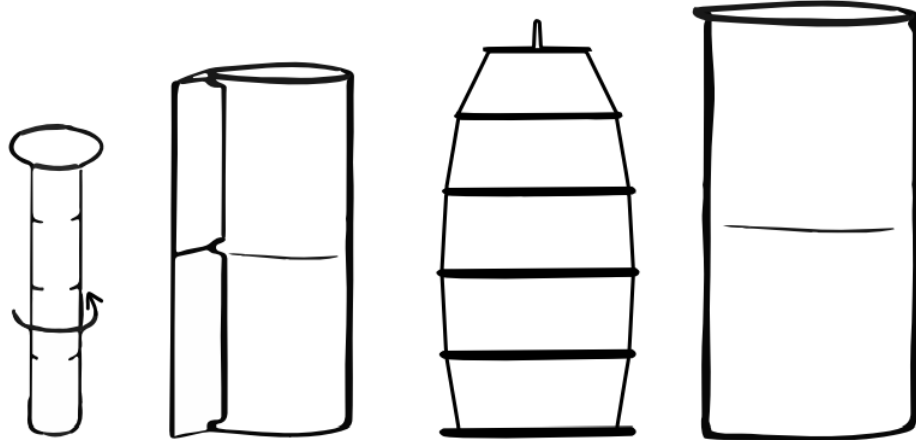


Figure 12. WAPS area proportions according to Table 5.

The WAPS lift comparison is used to design the rigid wing sails and the DynaRig, aiming at a similar savings as for one 30x5-m rotor sail. Instead of using the projected areas shown in Table 5 however, each rigid wing sail and the DynaRig are given a total projected sail area of 800 m². This simplifies the interpretation of the trends in the results. The area of the rotor sail remains at 150 m². All WAPS are installed at midship. Note that the vertical component of the CoE of each device is changed depending on their mast height.

The power savings are computed for each sailing and wind condition by subtracting the required delivered power of the wind-assisted ship (for each WAPS independently) from the conventional motor ship (without any WAPS onboard). Rotor RPM, sail AoA and d_{TF} are trimmed for each condition to maximize total power savings. The rotor's spinning power required and the air resistance (if applied) are accounted for. The program evaluates if an active WAPS produces more negative forward thrust than its own windage. In this condition, the WAPS is set to "reefed" (inactive) mode where windage is the only force component. Fig. 13 shows the power savings for all five different WAPS for the reference condition at 10 m/s TWS and 12.5 kn ship speed.

The percentage of savings of the total engine power required are for one WAPS of each type installed at mid-ship of the 'Maersk Pelican'. As a first order approximation, the results can be scaled to predict the savings when more devices are installed. However, interaction effects in the overall aerodynamic performance and non-linear hydrodynamic effects such as propeller efficiency, drag due to side force and rudder hydrodynamic side force play a key role and should be considered by conducting the performance predictions explicitly with all installed WAPS.

Considering the approximate nature of the model, the relative performance of each WAPS is discussed according to the results presented. All results presented in this section have heeling and leeway angles of less than 0.2° and 1°, respectively. These low values are the results of the wide beam of the Maersk Pelican and the single WAPS used in each run.

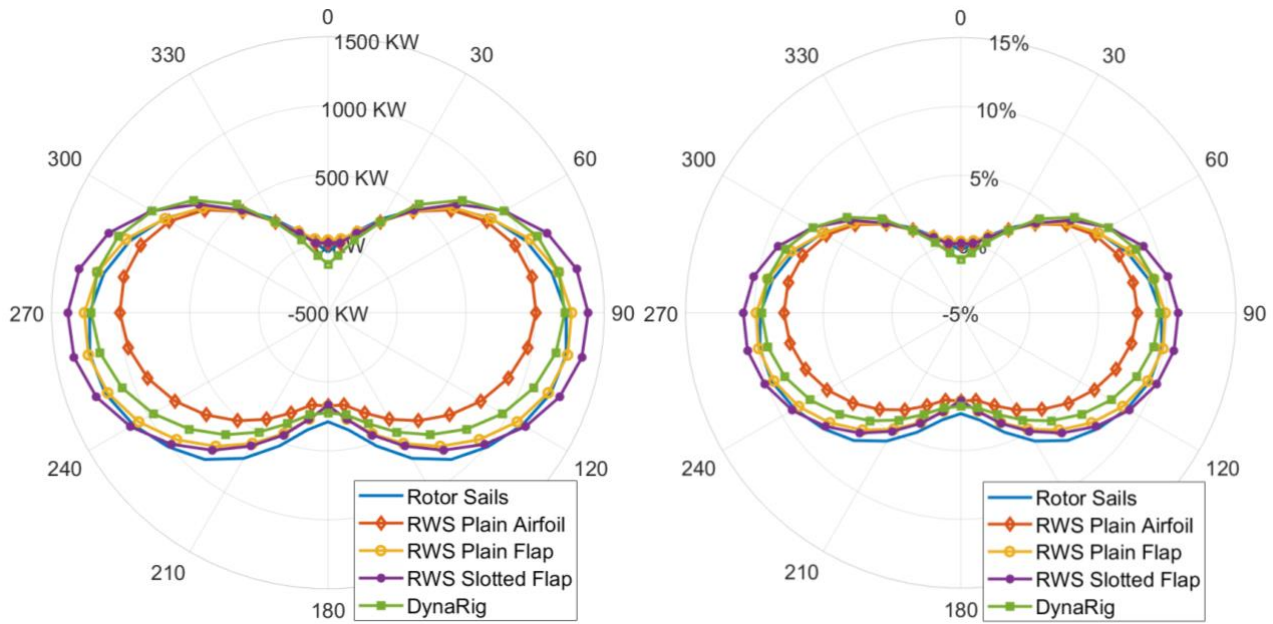


Figure 13. Power savings polar diagrams for all WAPS in reference service condition for Maersk Pelican (12.5kn Vs and 10m/s TWS) for TWA relative to the bow. Left, absolute power savings in kW. Right, power savings in percentage of the total engine power required.

Figure 13 shows how the maximum savings for all WAPS are very similar as intended by selecting the sail area of 800 m^2 . However, some differences between WAPS can be identified. Rotor sails are seen to perform better than the other WAPS in downwind ($TWA=180^\circ$) and broad reach ($TWA=135^\circ$) sailing courses. Trailing edge slotted and plain flaps can generate higher forward thrust than the plain airfoil, which leads to overall higher power savings for all TWAs. In pure downwind ($TWA=180^\circ$), all rigid wing sails perform equally since the AoA is set at 90° and the major component of the total aerodynamic force is drag. The DynaRig has higher potential in upwind ($TWA=45^\circ$) sailing courses where it outperforms the other configurations. For the non-retractable devices such as the DynaRig and the rotor sail, the air resistance effect is clearly seen at pure upwind condition ($TWA=0^\circ$) where savings are negative - the vessel must deliver higher power to overcome this resistance than without WAPS installed. For rotor sails sailing directly upwind, keeping the rotor spinning at $U/V \approx 1$ instead of turning it off and having only its windage component proved to achieve a better overall performance and, thus, higher power savings. At this low velocity ratio, the drag component is lower than its non-rotating air resistance thanks to the flow circulation (see Fig. 6 for reference).

To compare the WAPS performance for different wind conditions and same sailing speed of 12.5 kn, the TWS is firstly increased to 14 m/s. Then, it is reduced to 6 m/s. The results are shown in Figs. 14 and 15.

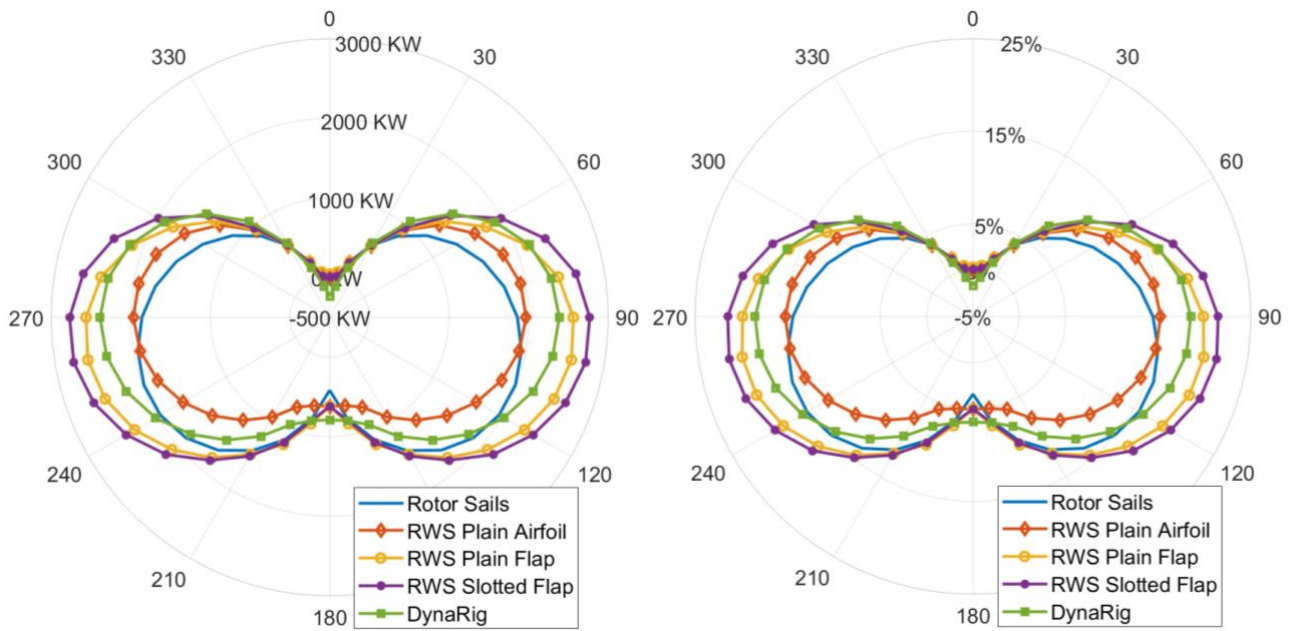


Figure 14. Power savings polar diagrams for all WAPS at 14m/s TWS and 12.5kn Vs for TWA relative to the bow. Left, absolute power savings in kW. Right, power savings in percentage of the total engine power required.

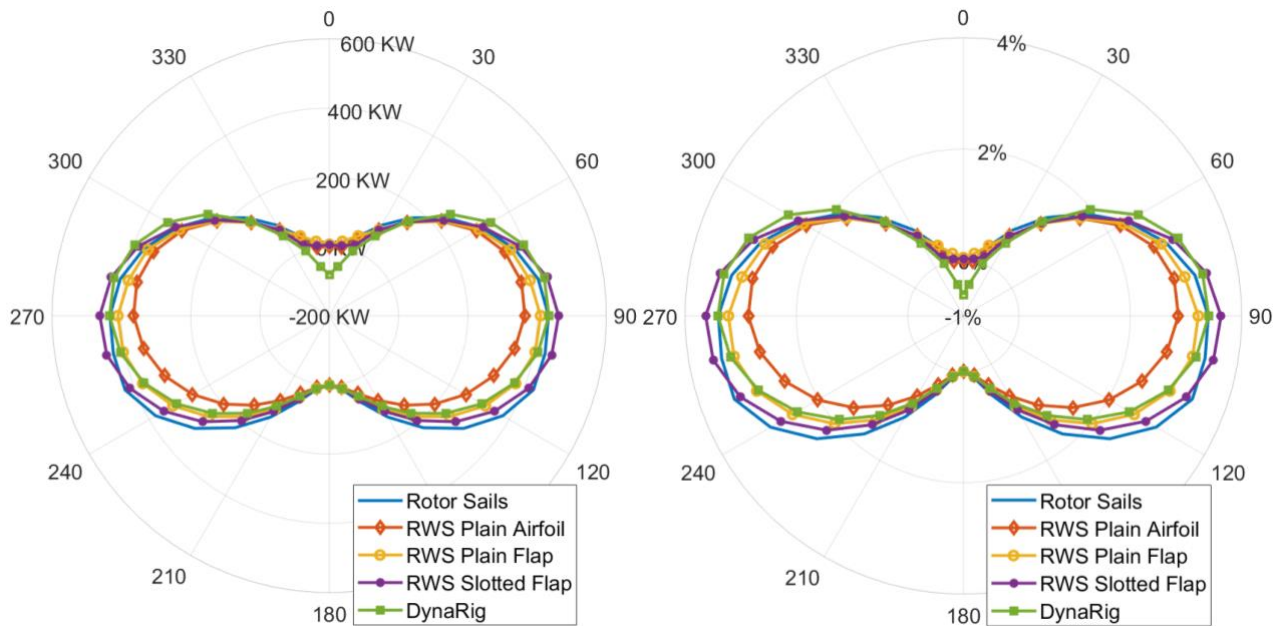


Figure 15. Power savings polar diagrams for all WAPS at 6m/s TWS and 12.5kn Vs for TWA relative to the bow. Left, absolute power savings in kW. Right, power savings in percentage of the total engine power required.

In Fig. 14, it is clearly shown how the rotor sail does not perform as well as the other WAPS for higher TWS. Due to its maximum spinning RPM limit (defined at 160 in this case according to Norsepower) and the increasing TWS, the rotor cannot reach the same high velocity ratio to achieve the highest lift coefficient. Thus, rotor sails tend to achieve lower power savings with increasing TWS than the other devices. On the contrary, theoretically, rigid wing sails and the DynaRig aerodynamic loads can increase quadratically as a function of AWS without limitations. However, they will have a real power limit due to ship stability and their own structural load limits. In this model, only ship stability has been considered. The maximum heel angle for the presented results is less than 0.2°.

For decreased TWS, as seen in Fig. 15, both power savings in absolute values and in percentage are reduced compared to the ones with higher TWS. However, same performance trends as for higher TWS are seen for all WAPS except the rotor sail. The rotor sail does not show depowering as it can reach the high lift coefficients while rotating at lower RPMs.

In another set of simulations, the TWS is kept at 10m/s while Vs is modified. Firstly, the ship speed is increased up to the maximum designed sailing speed of the “Maersk Pelican” of 15 kn. Then, it is reduced to 8 kn. The results are presented in Fig. 16 and 17.

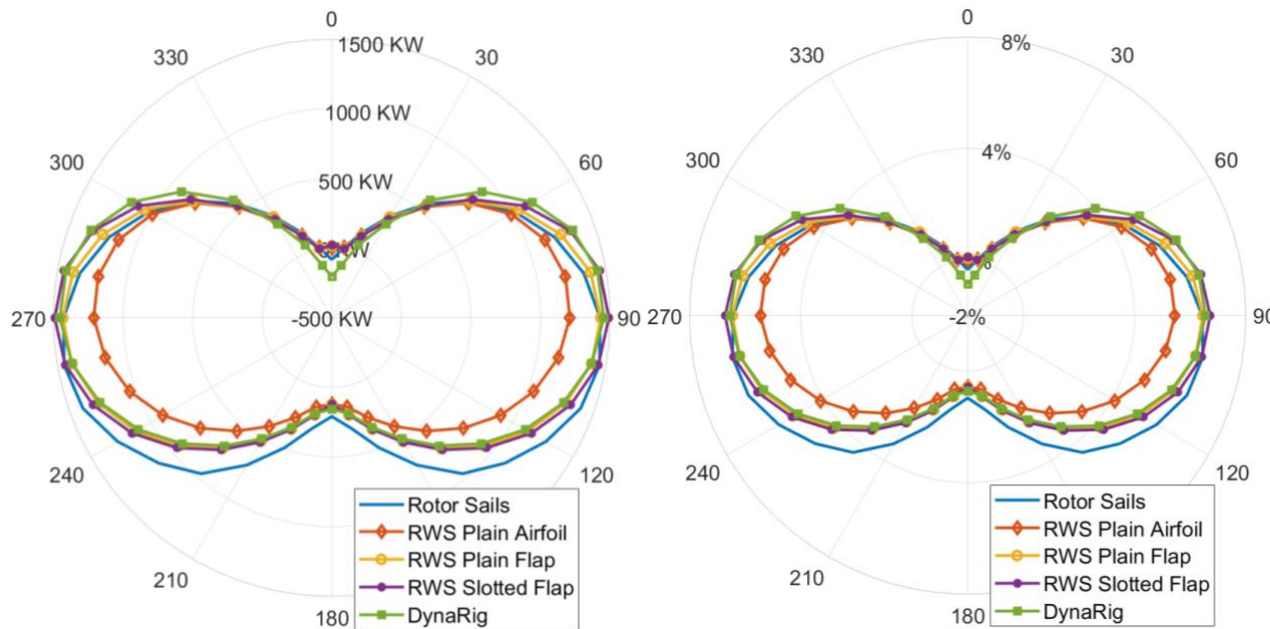


Figure 16. Power savings polar diagrams for all WAPS at 15kn Vs and 10m/s TWS for TWA relative to the bow. Left, absolute power savings in kW. Right, power savings in percentage of the total engine power required.

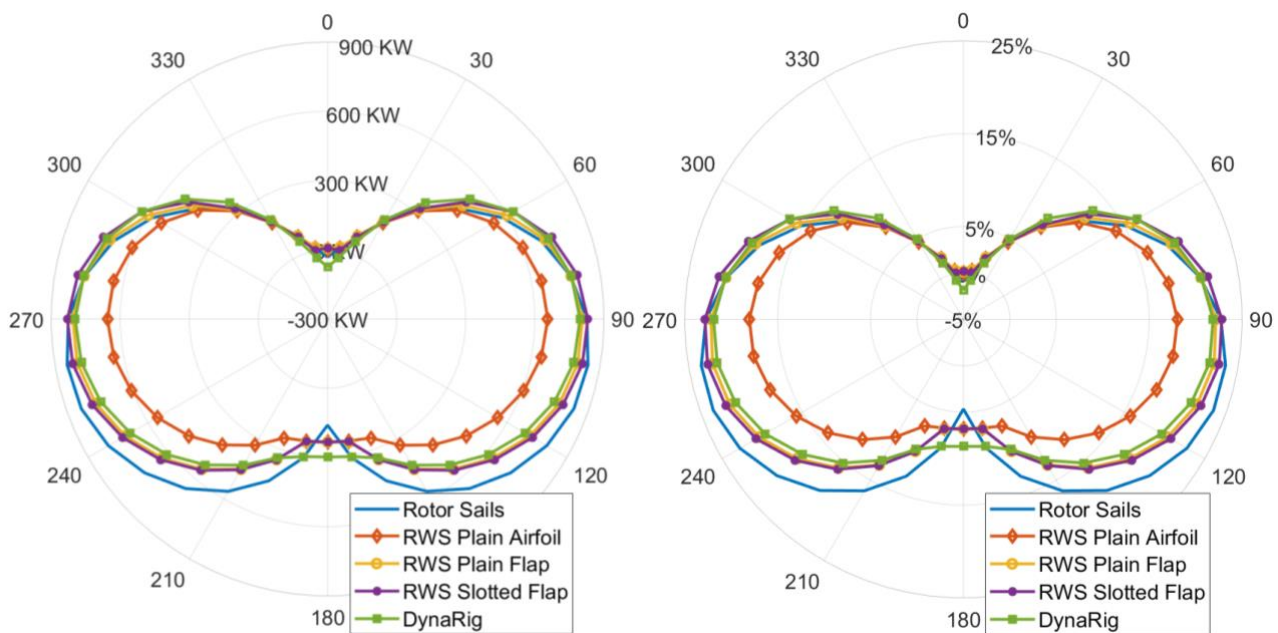


Figure 17. Power savings polar diagrams for all WAPS at 8kn of Vs and 10m/s TWS for TWA relative to the bow. Left, absolute power savings in kW. Right, power savings in percentage of the total engine power required.

In general terms, varying the sailing speed does not result in a difference in the relative performance of the WAPS, but it changes the magnitude of the savings. As shown in Fig. 16, when installing WAPS for increasing TWS , higher savings are achieved. On the other hand, as visible in Fig. 17, for decreasing service speed, a higher percentage of savings but lower absolute savings are achieved. This means that when sailing slower the WAPS does not generate higher forward thrust although its contribution results in a much higher percentage of the total engine power required.

7. CONCLUSIONS

The Performance Prediction Program (PPP) model presented in this paper allows for the fast assessment of the potential performance for three different WAPS which can currently be retrofitted on existing vessels and designed for new build vessels. Only the main particulars of the vessel and the generic configuration dimensions of the WAPS are required, so that the approach can be utilized during early stage feasibility studies. This generic approach is intended for high-level assessment of different concepts and should be followed by more in depth studies. While the WAPS models do not deliver a detailed performance description of a specific system implementation, this generic third-party assessment provides valuable insight for comparing concepts and evaluating general savings potentials.

The validation carried out shows good agreement with another performance prediction for the considered vessel, and fair agreement between real sailing data given all the measurement uncertainties. Once available, more full-scale data of wind-assisted ships could be studied and compared.

Rotor sails are found to be the most efficient WAPS studied on the basis of force generation per square meter of projected sail area. Considering the generic approach of the model presented, the results show that rotor sails perform better than the other WAPS in downwind and broad reach headings for the selected sailing conditions. On the other hand, the DynaRig shows high performance in upwind conditions while the rigid wing sail with trailing edge slotted flap performs best for a wide range of reaching wind angles. Also, it has been demonstrated how implementing trailing edge high lift devices in rigid wing sails improves the performance compared to the symmetric plain airfoil

The performance of the WAPS studied in different wind speeds are found to follow similar trends: higher absolute and percentage power savings are found with increasing TWS . However, rotor sails tend to achieve lower power savings with increasing TWS than the other devices, due to their limited maximum spinning RPM. Rigid wing sail and DynaRig power savings increase quadratically with AWS for the presented operating conditions. Nonetheless, they will have a power limits in strong winds due to heeling limitations and their own structural load limits, which could be implemented into future model developments. In the set of simulations carried out with varying ship speed, it is shown how varying the sailing speed changes the magnitude of the savings, but does not change the relative savings between the WAPS types. The WAPS does not generate higher forward thrust when sailing slower, but the contribution represents a much higher percentage of the total engine power required, and vice versa.

In the future, the model can be extended to include more WAPS such as Kites and Turbosails. To improve the accuracy of the model, sail-sail and sail-hull interaction effects on the aerodynamic performance could be introduced. Further research on the interaction effects between closely spaced devices is also needed. This would allow further optimization of WAPS design and performance. This model can provide valuable insight into the key role that WAPS can play in the quest for low-carbon shipping within the next few decades.

8. ACKNOWLEDGEMENTS

The authors would like to acknowledge the contribution of Ville Paakkari from Norsepower Oy Ltd, who provided the Maersk Pelican data for the validation of this Performance Prediction Program (PPP) for wind-assisted cargo ships.

9. REFERENCES

- Abbott, I. H., and Von Doenhoff, A. E. (1959). *Theory of Wing Sections*. Dover Publications, New York, USA.
- Bordogna, G. (2020). *Aerodynamics of Wind-Assisted Ships. Interaction Effects on the Aerodynamic Performance of Multiple Wind-Propulsion Systems*. PhD Thesis, Delft University of Technology.
- Bordogna, G., Muggiasca, S., Giappino, S., Belloli, M., Keuning, J., and Huijsmans, R. (2019). The Effects of the Aerodynamic Interaction on the Performance of Two Flettner Rotors. *Journal of Wind Engineering and Industrial Aerodynamics*, <https://doi.org/10.1016/j.jweia.2019.104024>.
- Bordogna, G., Muggiasca, S., Giappino, S., Belloli, M., Keuning, J., Huijsmans, R.H.M., and van't Veer, A.P. (2019). Experiments on a Flettner Rotor at Critical and Supercritical Reynolds Numbers. *Journal of Wind Engineering and Industrial Aerodynamics*, <https://doi.org/10.1016/j.jweia.2019.02.006>.
- Bradbury, W.M.S. (1981). An Investigation of Graduated Trim for an Aerofoil Rig. Proceedings of the Symposium on Wind Propulsion of Commercial Ships, 4-6 November, London, UK.
- Burden, A.B., Hearn, G.E., Lloyd, T.S., Mockler, S., Mortola, L., Shin, I.B., and Smith, B. (2010). Concept Design of a Fast Sail Assisted Feeder Container Ship. Proceedings of the Marine Unconventional Design Symposium, 8 July, London, UK.
- Chapin, V. (2015). Analysis, Design and Optimization of Navier-Stokes Flows around Interacting Sails. Proceedings of 5th High Performance Yacht Design Conference, 10-12 March, Auckland, NZ.
- Cousteau, J., Malavard, L., and Charrier, B. (1986). Apparatus for Producing a Force when in a Moving Fluid, United States Patent US4630997A.
- ENERCON (2013). Rotor Sail Ship E-Ship 1 Saves up to 25% Fuel. Enercon Press Release.
- Finck, R. D. (1977). USAF (United States Air Force) Stability and Control DATCOM. McDonnell Douglas Corporation, Douglas Aircraft Division, California, USA.
- Flettner, A. (1926). *Mein Weg zum Rotor*. Koehler & Amelang, Leipzig, DE.
- Hansen, H. (2008). Enhanced Wind Tunnel Techniques and Aerodynamic Force Models for Yacht Sails. PhD Thesis, The University of Auckland.
- Holtrop, J. (1977). A Statistical Analysis of Performance Test Results. *International Shipbuilding Progress*, 24(270), 23-28.
- Holtrop, J. (1984). A Statistical Re-Analysis of Resistance and Propulsion Data. *International Shipbuilding Progress*, 31(353), 272-276.
- Holtrop, J., and Mennen, G. G. J. (1978). A Statistical Power Prediction Method. *International Shipbuilding Progress*, 25(290), 253-256.

Holtrop, J., and Mennen, G. G. J. (1982). An Approximate Power Prediction Method. *International Shipbuilding Progress*, 29(329), 166–170.

Hooke, R., and Jeeves, T. (1961). Direct Search Solution of Numerical and Statistical Problems. *Journal of the Association for Computing Machinery*, Vol. 8, 212–229.

ITTC (1957). Skin Friction and Turbulence Stimulation. *8th International Towing Tank Conference* (ITTC). Madrid, Spain.

Kerwin, J.E. (1976). A Velocity Prediction Program for Ocean Racing Yachts. Proceedings of the New England Sailing Yacht Symposium, 24 January, New England, USA.

Kuiper, G. (1992). The Wageningen Propeller Series. *MARIN publication*, 92-001.

NASA (2015). Shape Effects on Drag. Available at: <https://www.grc.nasa.gov/www/k-12/airplane/shaped.html> (Accessed: 10th May 2020).

Newman, J. N. (2017). Marine Hydrodynamics; 40th Anniversary Edition. The MIT Press, Cambridge, USA.

Norsepower (2019). Norsepower Rotor Sails Confirmed Savings of 8.2% Fuel and Associated Co2 in Maersk Pelican Project [Press release]. 24th October. Available at: Confirmed Savings Of 8.2% Fuel And Associated Co2 In Maersk Pelican (norsepower.com) (Accessed: 9th December 2020).

Ouchi, K., Uzawa, K., Kanai, A., and Katori, M. (2013). "Wind Challenger" the Next Generation Hybrid Sailing Vessel. Proceedings of the 3rd International Symposium on Marine Propulsors, Launceston, AUS.

Paakkari, V., Hurford, A., and Craddock, C. (2020). Rotor Sail GHG Reduction Potential, Modelling and Sea Trial Data. Proceedings of the 5th Int. Conference on Innovation in High Performance Sailing Yachts and Sail-Assisted Ship Propulsion, 15-17 June 2020, Gothenburg, SE.

Perkins, T., Dijkstra, G., Perini-Navi, and Roberts, D. (2004). The Maltese Falcon: the Realisation. Proceedings of the 18th International HISWA Symposium on Yacht Design and Yacht Construction, 15-16 Nov. 2004, Amsterdam, NL.

Persson, A., Li, D.Q., Olsson, F., and Werner, S. (2019). Performance Prediction of Wind Propulsion Systems Using 3D CFD and Route Simulation. Proceedings of the International Conference on Wind Propulsion, 15-16 October, London, UK.

Prandtl, L., and Betz, A. (1932). Ergebnisse der Aerodynamischen Versuchsanstalt zu Göttingen; IV. Lieferung. Kaiser Wilhelm Institute for Fluid Dynamics, Göttingen, DE.

Prölls, W. (1963). Sailing Vessel with Square-Rigged Masts, United States Patent 3085539.

Rawson, K., and Tupper, E. (2001). Basic Ship Theory: Hydrostatics and Strength. Butterworth-Heinemann, Oxford, UK.

Rdurkacz (2013). Sketch of Magnus effect with streamlines and turbulent wake [Online image]. Wikimedia Commons. https://www.wikiwand.com/en/Magnus_effect#/.

Seifert, J. (2012). A Review of the Magnus Effect in Aeronautics. *Progress in Aerospace Sciences*, 55, 17-45.

Schenzle, P. (1980). Standardised Speed Prediction for Wind Propelled Merchant Ships. Proceedings of the Symposium on Wind Propulsion of Commercial Ships, 4-6 Nov. 1980, London, UK.

Schenzle, P. (1983). Wind as an Aid for Ship Propulsion. Proceedings of the West European Graduate Education in Marine Technology, 8th School "Ship Design for Fuel Economy", 29 Aug.-8 Sept. 1983, Gothenburg, SE.

Schenzle, P. (1985). Estimation of Wind Assistance Potential. *Journal of Wind Engineering and Industrial Aerodynamics*, 20, 97-110.

Schlichting, H. (1979). Boundary-Layer Theory. McGraw-Hill Book Company, New York, USA.

Smith, T., Newton, P., Winn, G., La Rosa, A.G. (2013). Analysis Techniques for Evaluating the Fuel Savings Associated with Wind Assistance. Proceedings of Low Carbon Shipping Conference, 9-10 Sept. 2013, London, UK.

Thom, A. (1934). Effect of Discs on the Air Forces on a Rotating Cylinder. *Aeronautical Research Committee Reports and Memoranda*, 1623.

Vahs, M. (2019). Retrofitting of Flettner Rotor - Results from Sea Trials of the General Cargo Ship "Fehn Pollux". Proceedings of the RINA International Conference on Wind Propulsion, 15-16 Oct. 2019, London, UK.

Van der Kolk, N. (2020). Sailing Efficiency and Course Keeping Ability of Wind Assisted Ships. PhD Thesis, Delft University of Technology.

Whicker, L., and Fehlner, L. (1958). Free-stream Characteristics of a Family of Low-Aspect Ratio, All Movable Control Surfaces for Application to Ship Design. *David Taylor Model Basin Report*, 933.

Young, A. D. (1953). The Aerodynamic Characteristics of Flaps. *Aeronautical Research Council Report and Memoranda*, 2622.